

THE DECELERATION OF GIANT HERBIG-HARO FLOWS

Elisabete M. de Gouveia Dal Pino¹

Received _____; accepted _____

arXiv:astro-ph/0012368v1 16 Dec 2000

¹Instituto Astronômico e Geofísico, Universidade de São Paulo, Av. Miguel Stéfano, 4200, São Paulo 04301-904, SP, Brasil; E-mail: dalpino@iagusp.usp.br

ABSTRACT

It has been recently discovered that spatially separated Herbig-Haro objects, once considered unrelated, are linked within a chain that may extend for parsecs in either direction of the embedded protostar forming a *giant Herbig-Haro jet*. Presently, several dozen of these giant flows have been detected and the best documented example, the HH 34 system, shows a systematic velocity decrease with distance on either side of the source. In this paper, we have modeled giant jets by performing fully three-dimensional simulations of overdense, radiatively cooling jets modulated with long-period ($P \sim$ several hundred years) and large amplitude sinusoidal velocity variability at injection ($\Delta v \sim$ mean jet flow velocity). Allowing them to travel over a distance well beyond the source, we have found that multiple travelling pulses develop and their velocity indeed falls off smoothly and systematically with distance. This deceleration is fastest if the jet is pressure-confined, in which case the falloff in velocity is roughly consistent with the observations. The deceleration occurs as momentum is transferred by gas expelled sideways from the traveling pulses.

The simulation of a pressure-confined, steady-state jet with similar initial conditions to those of the pulsed jet shows that the flow in this case experiences *acceleration*. This result is thus an additional indication that the primary source of deceleration in the giant flows *cannot* be attributed to braking of the jet head against the external medium.

Subject headings: Stars: pre-main-sequence - stars: mass loss - ISM:
jets and outflows - hydrodynamics

1. Introduction

The optical jets associated with low-mass, young stars have long been of interest. (For a review, see Reipurth & Raga 1999). First discovered over 15 years ago (Mundt & Fried 1983), these narrow strands of emission trace stellar winds that have been collimated in a bipolar fashion. The discrete Herbig-Haro knots along the jets are radiating shock fronts within this flow. Their bow shock morphology, high spatial velocity, and symmetric pattern with respect to the star (e.g., Zinnecker et al. 1998) all indicate that the shocks generally arise through the steepening of velocity fluctuations in the underlying, highly supersonic wind. Theoretical studies have confirmed that traveling shocks created in this manner reproduce the essential properties of the observed knots (Raga et al. 1990; Stone & Norman 1993; de Gouveia Dal Pino & Benz 1994).

Researchers at first considered the most luminous Herbig-Haro objects to be terminal bow shocks, i.e., to mark the location where the stellar wind impacts its cloud environment. However, these regions are typically displaced about 0.1 pc from the star, while the measured jet speeds are about 300 km s^{-1} . The corresponding travel time of 300 yr is a small fraction of the 10^5 yr period over which low-mass young stars are thought to drive vigorous winds (Adams, Lada, & Shu 1987). With the recent availability of wide-field CCD arrays, it has become clear that jets indeed extend to far greater distances. Spatially separated Herbig-Haro objects, once considered unrelated, are now seen to be links within a chain that may continue for parsecs in either direction from the embedded, central object.

The first clearly identified *giant Herbig-Haro flow* was the HH 34 system in the L1641 dark cloud of Orion A (Bally & Devine 1994). A Herbig-Haro object of that name had long been known (Herbig 1974), as had a well-delineated optical jet pointing back to the $45 L_{\odot}$ embedded source HH 34 IRS (Reipurth 1985). Wide-field imaging showed that about a dozen Herbig-Haro objects fall along a gentle S-curve centered on the star, and

extending over 1.5 pc. This linkage is not merely a visual impression. In a followup study, Devine et al. (1997) showed that all of the Herbig-Haro objects to the north of HH 34 IRS are redshifted, while the southern ones are all blueshifted. The actual radial velocities, moreover, decrease smoothly and systematically on either side of the star.

Since this initial discovery, several dozen additional giant flows have been found. All broadly resemble HH 34, but with conspicuous variations. Thus, the chain of Herbig-Haro objects centered on the HH 111 jet stretches nearly 8 pc from end to end, but exhibits very little bending (Reipurth et al. 1997). While the HH 34 flow has a low level of molecular emission near its ends, other systems, such as RNO 43, are encased within massive amounts of cloud gas and broad CO outflows (Bence et al. 1996). The HH 333 flow in the crowded field of NGC 1333 displays the usual S-curve, but is centered on an optically visible star (Bally et al. 1996).

These observations raise a number of important issues. How do jets maintain collimation over such extraordinary distances? What role do they play in dispersing the ambient cloud gas? What is the explanation for the S-shaped curves? Finally, why are the shocks slowing down?

On this paper, we embark on our own investigation of giant jets by focusing, at least initially, on the last question. The best documented example of deceleration is still the HH 34 jet, although the phenomenon has been seen in a number of others, such as HH 83, HH 335, RV Cep, and HH 111 (Reipurth et al. 1997). Figure 7 of Devine et al. (1997) shows that the radial velocities within both the north and south lobes of HH 34 decrease in a nearly linear fashion with distance, falling by at least a factor of 4 on either side of the driving star. Moreover, the measured rates of velocity decline are strikingly similar: $110 \text{ km s}^{-1} \text{ pc}^{-1}$ for the southern (blueshifted) lobe and $137 \text{ km s}^{-1} \text{ pc}^{-1}$ for the northern (redshifted) one. Proper motions of the most prominent optical knots also exhibit a falloff,

but the observational errors are too large for detailed comparison of the slopes.

The pattern of radial velocities argues that the deceleration is *not* created by braking against the external medium, which can hardly be expected to possess this degree of symmetry. In any case, the HH 34 jet projects into a region that is relatively depleted in molecular gas, as evidenced by the weak CO emission (Edwards & Snell 1984, Reipurth et al. 1986, Chernin & Masson 1995). The deceleration, therefore, must somehow be intrinsic to the flow itself. Both the proper motions and radial velocities in HH 34 are higher than the shock speeds deduced from emission lines (Bally & Devine 1997). This is the same pattern exhibited in shorter, contiguous jets, and demonstrates once more that the chain of bow shocks arises from velocity fluctuations in the underlying wind. Under what circumstances, then, do the shocks in a variable jet decelerate?

To address this question, we have modeled the jet through direct, numerical simulation. The brightest bow shocks within the giant flow must be created by order-unity changes of the wind velocity. Hence, our calculations simulate a jet modulated with large amplitude, and we allow material to travel an appropriate distance beyond the input source. The combination of large amplitude and computational length distinguishes our study from previous efforts. We find that the velocity near the central axis indeed falls systematically. This deceleration is fastest if the jet is pressure-confined, in which case the falloff in velocity is roughly consistent with the observations. The momentum lost by the axial matter is transferred to gas expelled sideways from the traveling pulses.

In Section 2 below, we detail the computational method employed in these simulations. Section 3 then presents numerical results. We stress from the outset that our study is limited in scope, and is not intended to simulate all aspects of the giant flows, nor to provide the coverage of parameter space that would be appropriate in a fuller treatment. Nevertheless, we feel that our calculations illustrate the basic principle that underlies

the observed deceleration. Finally, Section 4 discusses the observational and theoretical implications of our findings.

2. Computational Method

Our goal has been to study the behavior of a pulsed, radiatively cooled jet as it propagates into a medium of uniform density. For this purpose, we utilized a fully three-dimensional smoothed-particle hydrodynamics (SPH) code originally developed to investigate the working surfaces of steady jets (de Gouveia Dal Pino & Benz 1993). The code was subsequently employed, with appropriate modifications, to study low-amplitude, pulsing jets (de Gouveia Dal Pino & Benz 1994), propagation into stratified media (e.g., de Gouveia Dal Pino, Birkinshaw, & Benz 1996), de Gouveia Dal Pino & Birkinshaw 1996), momentum exchange processes with the environment (Chernin, Masson, de Gouveia Dal Pino, & Benz 1994), jet interactions with ambient clouds (de Gouveia Dal Pino 1999), and the effects of magnetic fields (e.g., Cerqueira, de Gouveia Dal Pino, & Herant 1997, Cerqueira & de Gouveia Dal Pino 1999). SPH is a Lagrangean, gridless approach to hydrodynamics, in which the equations of continuity, momentum, and energy are solved explicitly in time. Davies et al. (1993) have performed detailed comparisons of SPH calculations with those based on more traditional, finite-difference methods. In such tests, the two codes produce similar results although the spatial resolution of 3D-SPH may be sometimes inferior (see, e.g., de Gouveia Dal Pino 1999 and references therein for a detailed discussion of the basic assumptions of the method and accuracy criteria).

In this preliminary investigation of the giant HH jets, we have neglected the effects of magnetic fields. Lately, these have been the object of intensive numerical study in HH jets by several groups (see, e.g., de Gouveia Dal Pino & Cerqueira 1996, Stone, Xu & Hardee 1997, Cerqueira, de Gouveia Dal Pino & Herant 1997, Frank et al. 1998, Gardiner et al.

2000, O’Sullivan & Ray 2000, Stone & Hardee 2000, Cerqueira & de Gouveia Dal Pino 2000), despite the uncertainties related to their real strengths and topology. These studies have revealed that, while magnetic fields with reliable intensities and geometries generally improve the collimation of the flow and may significantly affect their detailed structure, particularly behind the shocks, they cause a minor influence on the dynamical structure of the beam in comparison to pure hydrodynamical calculations. Thus as in the present analysis we are focusing on the deceleration behaviour of the giant outflows, we may expect that the general results and conclusions of this work will not be very much affected by the inclusion of magnetic fields.

The computational domain is a three-dimensional, rectangular box, taken to represent the ambient medium. Within our Cartesian coordinate system, the box has dimensions $-50 R_j \leq x \leq 50 R_j$, $-9 R_j \leq y \leq 9 R_j$, $-9 R_j \leq z \leq 9 R_j$, where R_j is the initial jet radius (and R_j is the code distance unit). The origin of the coordinate system lies at the center of the box. The jet is continuously injected at $(-50 R_j, 0, 0)$ and subsequently flows in the x -direction. Within the box, 330,000 particles are initially distributed uniformly in space. The particles are smoothed out in space and the fluid quantities are derived by employing a spherically symmetric kernel function of width h . As in previous work, h was chosen initially to be $0.25 R_j$ and $0.50 R_j$ for the jet and ambient particles, respectively. The kernel width was then allowed to vary in space and time during subsequent evolution, in order both to optimize resolution in high-density regions, and to economize in the sparse, outer cocoon. (See also de Gouveia Dal Pino & Benz 1994; de Gouveia Dal Pino & Birkinshaw 1996). The code advances all quantities in time with a second-order, Runge-Kutta-Fehlberg integrator, and employs the Newman-Ritchmyer artificial viscosity to handle shocks. Outflow boundary conditions are assumed at the walls of the box.

We treat both the jet and the ambient gas as a fully ionized fluid that obeys an

ideal equation of state with $\gamma = 5/3$. Radiative cooling is due to collisional excitation and recombination. We adopt a local prescription, employing the cooling function of Katz (1989) for a gas of cosmic composition. For temperatures below 10^4 K, the assumption of complete ionization fails, and the density becomes optically thick to its own cooling radiation. Rather than deal with these complications, we have simply forced the cooling to zero in this regime. A consequence of this adiabatic approximation is that we underestimate the degree of clumping in relatively low-temperature regions. On the other hand, we have also neglected the ambient magnetic field, which should provide much of the supporting pressure in this regime (Hollenbach & McKee 1979). Our treatment of postshock clumping, while insufficient for a detailed study of the working surfaces (e.g., Blondin et al. 1990), should be adequate for the present purpose of describing the larger-scale momentum transfer between the jet and its environment.

The velocity of the jet at the circular inlet is given by

$$v_o(t) = v_j + \Delta v \sin\left(\frac{2\pi t}{P}\right) . \quad (1)$$

Here v_j is the mean jet speed, Δv the amplitude of velocity variations, and P their period. The models are also characterized by three additional, nondimensional parameters: (a) the initial density contrast between the jet and the ambient medium, $\eta \equiv n_j/n_a$, (b) the mean ambient Mach number, $M_a \equiv v_j/c_a$, where c_a is the ambient sound speed, and (c) the pressure ratio at the inlet, $\kappa \equiv p_j/p_a$.

3. Numerical Results

3.1. Pressurized Jets

We have chosen the parameters of our study to be representative of observed conditions within the giant Herbig-Haro flows. Where data were unavailable, we utilize observations

of the shorter, contiguous jets. As in previous studies, we fixed n_j , the input jet number density, at 600 cm^{-3} , a figure representative of estimates derived through shock modeling of the emission lines (e.g., Raymond et al. 1994). We further set the density contrast η equal to 3 in all our runs. Previous simulations for steady jets indicate that this figure yields a working surface for the leading bow shock that mimics the spatial clumping of such well-studied shocks as HH 1 and 2 (Blondin et al. 1990; de Gouveia Dal Pino & Benz 1993). Note that a significantly lower value of η (e.g., $\eta < 1$) results in a large, inflated cocoon behind the leading shock, while a much higher figure ($\eta > 10$) yields a dense, bullet-like working surface.

As our first numerical experiment, we consider a jet that is in pressure equilibrium with its surroundings, i.e., for which $\kappa = 1$. As in previous works, we choose the ambient temperature to be $T_a = 10^4 \text{ K}$, so that $c_a \equiv (\gamma k_B T_a / \bar{m})^{1/2} \simeq 17 \text{ km s}^{-1}$. Here, k_B is Boltzmann’s constant and \bar{m} the mean mass per particle. The corresponding temperature within the jet is $T_j = T_a \eta^{-1} \simeq 3300 \text{ K}$, while the sound speed is $c_j = c_a \eta^{-1/2} = 9.6 \text{ km s}^{-1}$. The temperature T_j is considerably lower than that in the postshock cooling regions that emit the observed optical emission lines, and should rather be viewed as an average between widely spaced shockfronts. In addition, our adopted T_a is far greater than any actual kinetic temperature within a molecular cloud. Nevertheless, our imposition of pressure equilibrium is reasonable, since observed jets spread much more slowly than their associated Mach angles (Ray & Mundt 1993). How this collimation is actually achieved remains an open question. If, as is widely believed, the collimating agent is the pinching force from a toroidal magnetic field component (e.g., Pudritz et al. 1991; Cerqueira & de Gouveia Dal Pino 1999, 2000; Gardiner et al. 2000), then our ambient pressure may be considered a surrogate for this effect. We discuss in the next subsection the consequences of relaxing the assumption of pressure balance.

We set both the jet’s mean velocity v_j and amplitude Δv to 100 km s^{-1} . These figures are appropriate for giant flows such as HH 34 (Devine et al. 1997). The mean ambient Mach number is therefore $M_a = v_j/c_a = 6$, and the maximum ambient and jet Mach numbers are $M_{a,max} = v_{j,max}/c_a \simeq 12$, and $M_{j,max} = v_{j,max}/c_j \simeq 21$, respectively. Also representative is the jet period, $P = 760 \text{ yr}$. The flow is injected into a circular inlet of radius $R_j = 10^{16} \text{ cm}$. The latter value is about a factor of 10 greater than the widths of jets much closer to the driving stars, as seen in HST images (e.g., Reipurth & Raga 1999). The more extended bow shocks in giant jets may indicate that the underlying flows are also broader, but there has been no quantitative study of this point. In any case, the jet width at the inlet does affect the detailed pattern of radiated emission, but not the gross dynamics of the jet-cloud interaction (de Gouveia Dal Pino & Benz 1993, Stone & Norman 1993). Note finally that the fiducial time unit in our study is that required for an ambient sound wave to traverse the jet radius. With the indicated choice of parameters, this unit is $t_d = R_j/c_a \simeq 190 \text{ yr}$.

Figure 1 displays these results at a time $t = 22t_d \simeq 4200 \text{ yr}$ after the initial injection (which corresponds to the beginning of a new period with the injection of a new pulse at the inlet). At this point, the jet has propagated for $100 R_j$, or almost 0.3 pc . The upper and lower panels show, respectively, the density contours and velocity vectors in the midplane ($z = 0$). The leading pulse or *working surface* is just leaving the right-hand border in both panels. This sharp feature is followed by 4 others, including the one just forming near the inlet. Since $P \approx 4t_d$, there has been time for 7 pulses to form through steepening of the input sinusoidal velocity profile. The first 3 of these have overtaken the leading one and merged with it. Each new pulse at the left forms within a time of about $3t_d$. This figure agrees with that previously obtained by Raga et al. (1990) and Raga & Canto (1998) in their analysis of steepening within a one-dimensional, sinusoidal injection profile.

The total propagation time for the HH 34 flow, from the star itself to the last visible shocks is about 10^4 yr (Devine et al. 1997). Such a period may be brief compared to the expected evolutionary time scale of the central source, whether it is a true protostar or a deeply embedded pre-main-sequence object. Thus, any results from simulations in which the leading pulse still plays a role are transients that should be viewed in this light. It is important to establish, for example, that the basic pattern seen in Figure 1 still holds even after the first bow shock has left the computational domain. Our results indicate that this is the case.

To illustrate the point, Figure 2 shows results from two different epochs, $t = 22t_d$ (as before) and $t = 24t_d \simeq 4600$ yr. The top two panels show the variation of longitudinal velocity v_x along the jet’s central axis, while the bottom two display the run of central density. We see that the velocity profile exhibits the saw-tooth pattern familiar from earlier, one-dimensional studies of free-streaming oscillating jets (e.g., Raga & Kofman 1992). At the later time, each embedded peak shifts to the right, but the overall pattern remains. The central density has pronounced spikes at each velocity minimum, i.e., just behind the leading shock within each pulse. ²

The lower left panel of Fig. 2 ($t = 22t_d$) also shows that, in the beginning of each period, when a new pulse forms at the jet inlet, its density is initially high, due to the efficient radiative cooling of the shocked material, and then decreases as the pulse propagates. (At $t = 22t_d$, the new pulse has an initial density $\sim 65n_a$ which decreases to $\sim 9n_a$ at $t = 24t_d$, in the lower right panel.) In fact, at both epochs, the downward

²The pulses formed by the steepening of velocity in a variable jet consist of two shock fronts moving in tandem (e.g., Hartigan & Raymond 1993). Our simulations only resolve the two fronts within the first few pulses, where they appear as breaks within the steep velocity declines in Figure 2.

sharp density spikes fall off in the downstream direction. This effect has been studied in previous numerical work (see, e.g., de Gouveia Dal Pino & Benz 1994, Völker et al. 1999), and is consistent with measurements of electron density decay with distance in HH jets (e.g., Reipurth 1999). The initial velocity differences impressed on the flow at the inlet are gradually erased as faster material catches up with slower, upstream gas thus producing the saw-tooth pattern. The peak velocities are falling off with distance in a nearly linear fashion (by a factor ~ 2 within ~ 0.3 pc).

In our simulation, we also find that the propagation speed of each pulse (or internal working surface, WS), v_{WS} , diminishes, although at a slower rate. Figure 3 plots this speed at the same two epochs. Here we derived v_{WS} by differencing the position of the density spike at closely spaced times. The segmented nature of the curves results from the fact that this velocity has been computed only for some specific positions of the density spikes. Note that the severe, final drop in v_{WS} at $t = 22 t_d$ represents the deceleration of the leading bow shock, as it sweeps aside warm, ambient gas. In fact, its propagation velocity which is initially $v_{\text{WS},o} \simeq v_{j,max}/[1 + \eta^{-1/2}] \simeq 7.5 c_a \sim 126 \text{ km s}^{-1}$ (e.g., de Gouveia Dal Pino & Benz 1993), decreases to $v_{\text{WS},o} \sim 3.5 c_a$ at $t = 22 t_d$, just before it leaves the computational domain, as indicated in Fig. 3 (top panel). The results above are in qualitative agreement with the observed kinematics of HH34 system for which a deceleration factor ~ 1.5 has been observed within the same distance.

Fig. 3 also depicts the calculated propagation velocity of the internal pulses along the jet’s central axis which was estimated under the assumption that each pulse traps only a small amount of gas between its two shocks (and eject most of the material sideways). In this case, the motion of an internal pulse is obtained from the balance between the pre and post pulse momentum fluxes (neglecting the gas pressures up- and down-stream) which

gives (see, e.g., Raga & Kofman 1992, de Gouveia Dal Pino & Benz 1994):

$$v_{WS,cal} \sim \frac{(\rho_l/\rho_r)^{1/2}v_l + v_r}{(\rho_l/\rho_r)^{1/2} + 1} \quad (2)$$

where v_l and v_r are the flow velocities, and ρ_l and ρ_r are the densities immediately up- and down- stream of each pulse, respectively. Substituting in the equation above the measured values from the simulation for ρ_l/ρ_r , v_l , and v_r for each pulse (see Fig. 2) we have derived the dashed curves of Fig. 3. Eq. (2) which is valid for one-dimensional shocks under the conditions described above should be applicable to the jet axis of Fig. 1, where the shock velocity is mostly parallel to the jet axis. The slight disagreement of the dashed curves in Fig. 3 with the propagation velocities measured in the simulations (solid curves) is caused by the fact that some amount of momentum is escaping sideways, even from the central region.

Figure 4 displays the variation of momentum flow at the time $t = 24t_d$. The dashed curves are profiles of the momentum flux, ρv_x^2 , shown as a function of the transverse coordinate y . Each profile is computed at the x -position where the flux asymptotes to zero. Comparing with Figure 2, we see how the momentum flux rises at the position of each pulse, and then falls in between. The actual peak value of ρv_x^2 systematically declines, an indication that the jet is losing momentum.

The solid curves in the panel show the momentum transport rate, represented by the quantity $\int_0^y \rho v_x^2 y dy$. Since the flow is nearly symmetric about the central axis, we may replace y by $r/\sqrt{2} \equiv [(y^2 + z^2)]^{1/2}$ in the integral, which is then proportional to the momentum per unit time crossing within a circle of radius r at each x -position. The curves are shallowest between pulses, where the least momentum flow occurs. Conversely, they are deepest at the pulses themselves. Their depth at the pulse positions declines from the first pulse (near the inlet) to the last one shown. In other words, *the full momentum transport rate is lower at the far end than at the inlet*. The excess momentum must be taken up by

whatever mass leaves the box, i.e., by the external medium.

3.2. Overpressured Jets

We next consider a jet that is injected with significantly higher pressure than its surroundings. Retaining $\eta = 3$ and $n_j = 600 \text{ cm}^{-3}$, we now lower the ambient temperature T_a to 10^3 K . We further take the initial temperature of the jet itself to be $T_j = 10^4 \text{ K}$. Thus, the new pressure ratio is $\kappa = \eta T_j / T_a = 30$. Our input velocity profile is still given by equation (1), with $v_j = \Delta v = 100 \text{ km s}^{-1}$, but we lower P slightly to 600 yr. Since the ambient sound speed is now only 5.3 km s^{-1} , the corresponding mean ambient Mach number is higher: $M_a \equiv v_j / c_a = 19$, $M_{a,max} = v_{j,max} / c_a \sim 38$, and $M_{j,max} = v_{j,max} / c_j \simeq 12$, with $c_j \simeq 16.6 \text{ km s}^{-1}$. The fiducial crossing time is now raised to $t_d = R_j / c_a \simeq 600 \text{ yr}$. Thus, we now have $P = t_d$.

Figure 5 shows density contours in the midplane for $t = 2 t_d \simeq 1200 \text{ yr}$, $t = 4 t_d \simeq 2400 \text{ yr}$, and $t = 6 t_d \simeq 3600 \text{ yr}$. The later frame shows the jet just before the leading bow shock exits the computational boundary. In comparison with the upper panel of Figure 1, we see that the flow has expanded more rapidly in the transverse direction. One point in common is that, although there has been time to form 7 pulses, only 4 are visible. As before, 3 of the pulses originally formed have overtaken the leading bow shock and merged with it. ³

³ We note that in this particular case of the overpressured jet where the rapid transverse expansion could introduce undesirable boundary effects in the evolution of the flow, we made previous tests by simulating a shorter jet propagating in a computational domain with much larger transverse boundaries and an agreement better than 15% was found with the results of the narrower boundary simulation.

The variations in velocity and density along the central axis are displayed, respectively, in the top and bottom panels of Figure 6. Here we chose as representative times $t = 6t_d \simeq 3600$ yr, and $t = 9t_d \simeq 5400$ yr. Although the overall velocity profile still approximates a saw-tooth pattern, the peak value of v_x declines more slowly than before, except for the steep drop associated with the leading bow shock at the early time. The density spikes show no falloff at this epoch. Note especially the large pileup in mass just behind the leading bow shock. By $t = 9t_d$, the density spikes again decline, although somewhat erratically. The propagation speed of the pulses also displays no simple pattern (Fig. 7). The leading bow shock is slowing down by nearly the same rate as the jet flow, from an initial value $v_{WS,o} \simeq 22c_a \sim 126$ km s⁻¹ to $v_{WS,o} \simeq 14c_a \simeq 80$ km s⁻¹ at $t = 6t_d$, but the velocity of propagation of the internal pulses, v_{WS} , approximates the peak velocities of Fig. 6. We note also in Fig. 7 that the predicted propagation velocities of the internal pulses in the jet axis by eq. 2 (dashed lines) are now in less agreement with the measured values from the simulations than in the pressure-confined jet, thus suggesting that the condition of a negligible amount of gas being trapped between the shocks of each pulse is less sustained here.

Figure 8 displays the variation of momentum flow at the time $t = 9t_d$. As in Fig. 4, the dashed curves are profiles of the momentum flux, ρv_x^2 , shown as a function of the transverse coordinate y , and the solid curves show the momentum transport rate at each x -position. Again, the depth of the profiles rises and falls at pulse and interpulse locations, respectively, and the curves very near the pulses become shallower with increasing x (although more irregularly than in the case of the pressure-confined jet) thus indicating that momentum transport rate is lower at the far end than at the inlet.

The smaller deceleration rate of the overpressured jet is primarily related to the lesser ability of the cold ambient medium in slowing down this higher Mach-number jet. Besides,

although, like the pressure-confined jet of Fig. 1, it is progressively losing momentum sideways behind each internal pulse which causes deceleration, the jet is also undergoing an expansion specially near the inlet (due to the overpressure). This causes the development of crossing shocks that propagate from the edge of the beam inwards and produce partial refocusing of the sideways expanding material to the axis thus inhibiting the deceleration process.

3.3. Steady Jet

In order to test the importance of the primary impact of the pressure confined jet into the ambient medium, we also performed a numerical experiment considering a steady jet with the same input conditions of the pressure-confined jet of Fig. 1, but injected with a constant velocity $M_a = v_j/c_a \simeq 12$. Figure 9 depicts this steady jet just before it exits the computational domain, at $t \simeq 11t_d$, and Figure 10 displays the propagation velocity of the leading working surface at the jet's central axis as a function of the distance. We note that, instead of being decelerated by the impact with the warm ambient medium, the steady jet is first accelerated and then reaches a constant velocity regime. The dashed curve gives the predicted propagation velocity of the leading working surface in the case that the jet radius at the head (R_h) is $R_h \simeq R_j$, i.e., $v_{WS,o} \simeq v_j/[1 + (\eta\alpha^{-1/2})] \simeq 7.5 c_a \sim 126 \text{ km s}^{-1}$, where $\alpha = (R_j/R_h)^2 \simeq 1$ (e.g., de Gouveia Dal Pino & Benz 1993). The acceleration effect in Fig. 10 has been previously reported for radiatively cooling, overdense steady-state jets (de Gouveia Dal Pino & Benz 1993) and, according to the equation above, is directly related to the progressive decrease of the radius at the head as the jet propagates downstream (see Fig. 9). This result indicates that the deceleration observed in giant jets *cannot* be simply attributed to the impact of the leading working surface with the ambient medium. It is due instead to the momentum transfer by the gas expelled sideways by the multiple working

surfaces to the ambient medium as we have seen in the previous paragraphs.

4. Discussion and Conclusions

We have performed fully three-dimensional simulations of overdense, radiatively cooling jets evaluated for a set of parameters which are appropriate to giant protostellar jets.

Modeling jets with long-period ($P \sim$ several hundred years) and large amplitude sinusoidal velocity variability at injection ($\Delta v =$ mean jet flow velocity), and allowing them to travel over a distance well beyond the source, the injected sinusoidal flow velocity profile steepens into a saw-tooth pattern, in agreement with previous theoretical work (e.g., Raga & Koffman 1992, Völker et al. 1999), developing a chain of travelling internal pulses. For a pressure-confined jet (Figs. 1 to 4), the density spikes behind each pulse decrease as they propagate away from the source. Also, we find that the peak velocities of the saw-tooth flow and the propagation velocity of the internal pulses fall off with distance by a factor $\lesssim 2$ within ~ 0.3 pc, which is consistent with the observed kinematics of the HH34 system within the same distance. This deceleration is slower for an overpressured jet with similar input conditions but higher Mach number (Figs. 5 to 8). The analysis of the momentum flux along the flow and the total momentum rate crossing laterally the jet radius indicates that the deceleration in the pulsed giant jets is mainly caused by systematic momentum transfer sideways by the traveling pulses to the ambient medium.

We note that, in a previous work (Chernin et al. 1994), we have investigated numerically the possible processes of momentum transfer from astrophysical jets to the ambient medium and found that, while low Mach number (smaller than or equal to 6) jets slow down rapidly because they entrain turbulently ambient material along their sides, high Mach number beams, like the HH jets studied here, on the other hand, transfer

momentum to the ambient medium principally at the working surfaces (i.e., through "prompt" entrainment). The results of the present work are, therefore, consistent with this former analysis.

Also, the simulation of a pressure-confined steady-state jet (Figs. 9 and 10) with the same initial conditions of the pressure-confined pulsed jet above has shown that the steady jet experiences some acceleration, which is an additional indication that the primary source of the deceleration observed in the giant jets could not be attributed to braking of the leading bow shock against the ambient medium.

In a recent work, Cabrit & Raga (1999) utilizing a very simple analytical model have hypothesized that the observed jet deceleration in the HH 34 system could be possibly the result of drag forces of the ambient medium on individual jet knots arising from fragmentation of a time-variable, precessing jet. As we argued earlier, the symmetric pattern of deceleration in both lobes of the jet indicates that the process is rather internal to the flow. Our three-dimensional simulations show, in fact, that deceleration can be naturally produced in jets formed by long-period, large-amplitude velocity variations, where momentum is progressively lost from the central axis and transferred sideways by the travelling pulses.

Finally, we note that, for the sake of simplicity and also because observations offer only average estimates, we have assumed in this study an initially homogeneous ambient medium, although we could expect some stratification in density and temperature, and even in pressure, of the environment surrounding the giant flows. Previous numerical studies involving stratified ambient media have been done both in the context of extragalactic jets (see, e.g., Wiita et al. 1990, Hardee et al. 1992), and the shorter protostellar jets (see, e.g., de Gouveia Dal Pino, Birkinshaw, & Benz 1996, de Gouveia Dal Pino & Birkinshaw 1996), but in the future, a more complete analysis of the giant flows must include a stratified

ambient medium for a complete investigation of its effects upon the structure and long term evolution of the flow over the cloud. For example, for an overdense jet, as long as the pressure is maintained constant, one could expect that ambient density and temperature variations by, say a factor of two or so, while having a minor effect on the jet dynamics, they could more significantly affect the radiative emission structure of the shocks (due to the strong dependence of the radiative cooling distance with the shock velocity and thus with the density ratio between the jet and the ambient medium; see, e.g., de Gouveia Dal Pino & Benz 1993).

This work has benefited from several valuable and enthusiastic discussions and profitable comments from S. Stahler, F. Shu, and A. Raga, during my visit to the University of California at Berkeley. I am particularly indebted to S. Stahler who suggested the original idea of this work. This work has been partially supported by grants of the Brazilian agencies FAPESP and CNPq.

REFERENCES

- Adams, F.C., Lada, C.J., & Shu, F.H. 1987, *ApJ*, 312, 788
- Bally, J., & Devine, D. 1994, *ApJ*, 428, L65
- Bally, J., Devine, D., & Reipurth, B., 1996, *ApJ*, 473, L49
- Bence, S.J., Richer, J.S., & Padman, R. 1996, *MNRAS*, 279, 866
- Blondin, J.M., Fryxell, B.A., & Königl, A. 1990, *ApJ*, 360, 370
- Cabrit, S., & Raga, A. C. 1999, *A&A*,
- Cerqueira, A.H. & de Gouveia Dal Pino, E.M. 1999, *ApJ*, 510, 828
- Cerqueira, A.H. & de Gouveia Dal Pino, E.M. 2000, *ApJ*(submitted)
- Cerqueira, A.H., de Gouveia Dal Pino, E.M., & Herant, M. 1997, *ApJ*, 489, L185
- Chernin, L., & Masson, C. 1995, *ApJ*, 443, 181
- Chernin, L., Masson, C., de Gouveia Dal Pino, E.M. & Benz, W. 1994, *ApJ*, 426, 204
- Davies, M.B. et al. 1993, *A&A*, 272, 430
- de Gouveia Dal Pino, E.M. 1999, *ApJ*, 526, 862
- de Gouveia Dal Pino, E.M. & Benz, W. 1993, *ApJ*, 410, 686
- de Gouveia Dal Pino, E.M. & Benz, W. 1994, *ApJ*, 435, 261
- de Gouveia Dal Pino, E.M., & Birkinshaw, M. 1996, *ApJ*, 471, 832
- de Gouveia Dal Pino, E.M., Birkinshaw, M. & Benz, W. 1996, *ApJ*, 460, L111
- de Gouveia Dal Pino, E.M., & Cerqueira, A.H. 1996, *Astrophys. Lett. Comm.*, 34, 303

- Devine, D., Bally, J., Reipurth, B., & Heathcote, S. 1997, *AJ*, 114, 2095
- Edwards, S., & Snell, R.L. 1984, *ApJ*, 281, 237
- Frank, A., Ryu, D., Jones, T.W., & Noriega-Crespo, A., 1998, *ApJ*, 494,L79
- Gardiner, T.A., Frank, A., Jones, T.W., & Ryu, D. 2000, *ApJ*, 530, 834
- Hardee, P.E. et al. 1992, *ApJ*, 387, 460
- Hartigan, P., & Raymond, J. 1993, *ApJ*, 409, 705
- Herbig, G.H. 1974, *Lick Obs. Bull.*, N. 658
- Hollenbach, D.J., & McKee, C.F. 1979, *ApJS*. 41, 555
- Katz, J. 1989, PhD Thesis, Princeton Univ.
- Mundt, R., & Fried, J.W. 1983, *ApJ*, 274, L83
- O’Sullivan, S., & Ray, T.P. 2000, *A&A* (in press)
- Raga, A.C., Canto, J. 1998, *RevMexAA*,
- Raga, A.C., & Kofman, L. 1992, *ApJ*, 386, 222
- Raymond, J. C. et al. 1994, *ApJ*, 434, 232
- Reipurth, B. 1985, *A&A*, 61, 319
- Reipurth, B. 1999, in "Herbig-Haro Objects and their Energy Source", Copenhagen Univ. Astron. Observ., Niels Bohr Inst. (Kopenhagen), p. 72
- Reipurth, B., et al. 1986, *A&A*, 164, 51
- Reipurth, B., Bally, J., & Devine, D., 1997, *AJ*, 114, 2708

- Reipurth, B., & Raga, A.C. 1999, in *The Origin of Stars and Protoplanetary Systems*, eds. Charles Lada & Nikolaos D, Kylafis, p.
- Reipurth, B., Raga, A.C., & Heathcote, S. 1996, *A&A*, 311, 989
- Stone, J.M., & Hardee, P.E. 2000, *ApJ*(in press)
- Stone, J.M., & Norman, M. 1993, *ApJ*, 379, 676
- Stone, J.M., Xu, J., & Hardee, P.E. 1997, *ApJ*, 483, 121
- Völker, R., Smith, M.D., Suttner, G., & Yorke, H.W. 1999, *A&A*, 343, 953
- Wiita, P.J., Rosen, A., & Norman, M.L. 1990, *ApJ*, 350, 545
- Zinnecker, H., McCaughrean, M., & Rayner, J. 1998, *Nature*, 394, 862

FIGURE CAPTIONS

Figure 1: Mid-plane density contour (top) and velocity field distribution (bottom) for a pressure-confined radiatively cooling, pulsed jet propagating into a warm ambient medium with $T_a \sim 10^4$ K. The sinusoidal velocity variability at injection has a period $P \sim 4t_d \sim 764$ yr (where $t_d = R_j/c_a \approx 190$ yr, and $R_j = 10^{16}$ cm), a mean speed $v_j = 100\text{kms}^{-1}$, and an amplitude $\Delta v = 100\text{kms}^{-1}$. The time depicted is $t/t_d \sim 22 \sim 4200$ yr, and the jet has propagated for $100 R_j \sim 0.3$ pc. The initial conditions for the jet are: $\eta = n_j/n_a = 3$, $n_a = 200 \text{ cm}^{-3}$, $M_{a,max} = 12$, and pressure equilibrium in the jet at the inlet, $\kappa = p_j/p_a = 1$. The distances are in units of $R_j = 10^{16}$ cm. The density lines are separated by a factor of 1.3 and the density scale covers the range $\sim (1.3 \times 10^{-2} - 0.7 \times 10^2)n_a$.

Figure 2: Flow velocity (top) and density (bottom) profiles along the jet axis for the jet of Fig. 1, at $t/t_d = 22$ (left), and $t/t_d = 24$ (right). The flow velocity is in units of the ambient sound speed, $c_a \simeq 16.6 \text{ km s}^{-1}$, the density is in units of the ambient density $n_a = 200 \text{ cm}^{-3}$, and the distance is in units of $R_j = 10^{16}$ cm.

Figure 3: Propagation velocity of the leading and internal working surfaces, v_{WS} (in units of $c_a = 16.6\text{kms}^{-1}$), for the jet of Fig. 1 at $t/t_d \simeq 22$, and 25. The distance is in units of $R_j = 10^{16}$ cm.

Figure 4: Longitudinal component of the momentum flux density (dashed lines) and the integrated momentum rate distribution (solid lines) for the jet of Figs. 1 to 3, at $t/t_d \simeq 24$, in different positions along the flow. At the positions: $x/R_j = -29, -7, 16$, and 36 , the lines trace the distributions profiles immediately behind the pulses; at the other positions, they trace the distributions at regions between the pulses. The momentum flux density, and the momentum rate scales can be calibrated using the markers in the top region of each plot - the marker for the momentum flux density corresponds to $\sim 2.9 \times 10^{-18} \text{ g cm}^{-3} (\text{km s}^{-1})^2$, and the marker for momentum rate corresponds to $\sim 1.4 \times 10^{-6} M_\odot \text{ yr}^{-1} \text{ km s}^{-1}$.

Figure 5: Mid-plane density contour evolution of an overpressured radiatively cooling, pulsed jet propagating into an ambient medium with $T_a \sim 10^3$ K. The sinusoidal velocity variability at injection has a period $P \sim 1t_d \sim 604$ yr (where $t_d = R_j/c_a \approx 604$ yr, and $R_j = 10^{16}$ cm), a mean speed $v_j = 100$ km s $^{-1}$, and an amplitude $\Delta v = 100$ km s $^{-1}$. The times depicted are $t/t_d \sim 2 \sim 1200$ yr, $t/t_d \sim 4 \sim 2400$ yr, and $t/t_d \sim 6 \sim 3600$ yr. The initial conditions for the jet are: $\eta = n_j/n_a = 3$, $n_a = 200$ cm $^{-3}$, $M_{a,max} \sim 38$, and a jet to ambient pressure ratio at the inlet $\kappa = p_j/p_a \sim 30$, with an initial jet temperature $T_j = 10^4$ K. The distance is in units of $R_j = 10^{16}$ cm. The density lines are separated by a factor of 1.3 and the density scale covers the range $\sim (1.1 \times 10^{-2} - 0.51 \times 10^2) n_a$ at $t/t_d \sim 2$, $\sim (1.2 \times 10^{-2} - 0.5 \times 10^2) n_a$ at $t/t_d \sim 4$, and $\sim (1.1 \times 10^{-2} - 0.99 \times 10^1) n_a$ at $t/t_d \sim 6$.

Figure 6: Flow velocity (top) and density (bottom) profiles along the jet axis for the jet of Fig. 5, at $t/t_d \sim 6$ (left), and $t/t_d \sim 9$ (right). The flow velocity is in units of the ambient sound speed, $c_a \simeq 5.25$ km s $^{-1}$, the density is in units of the ambient density $n_a = 200$ cm $^{-3}$, and the distance is in units of $R_j = 10^{16}$ cm.

Figure 7: Propagation velocity of the leading and internal working surfaces, v_{WS} (in units of $c_a = 5.25$ km s $^{-1}$), for the jet of Fig. 5 at $t/t_d \simeq 6$, and 9. The distance is in units of $R_j = 10^{16}$ cm.

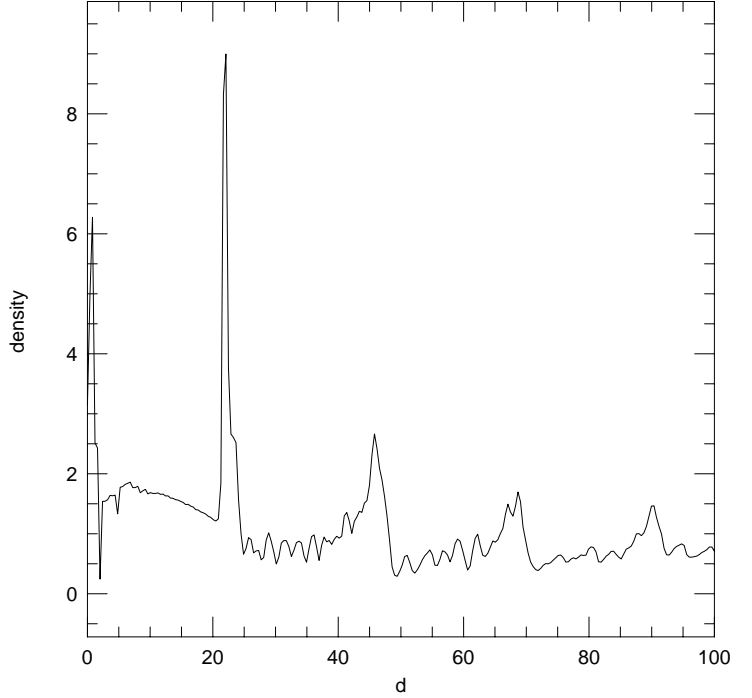
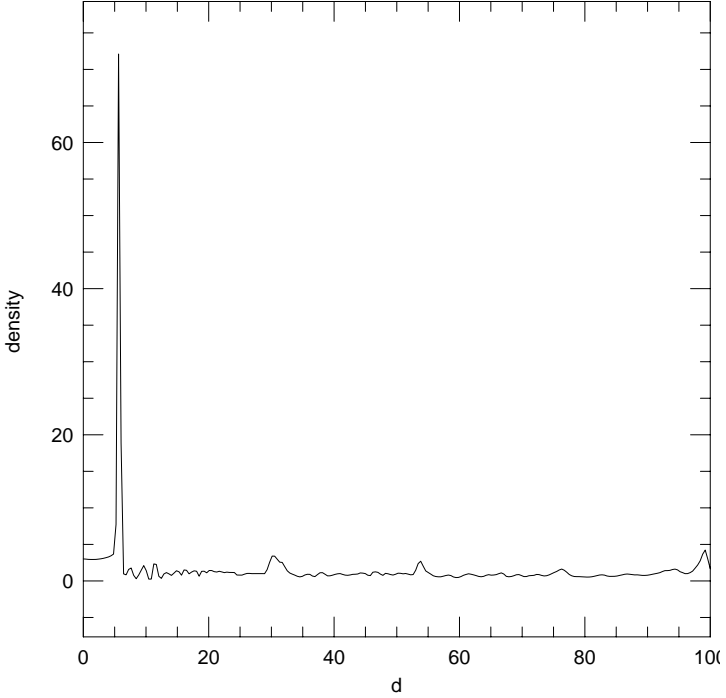
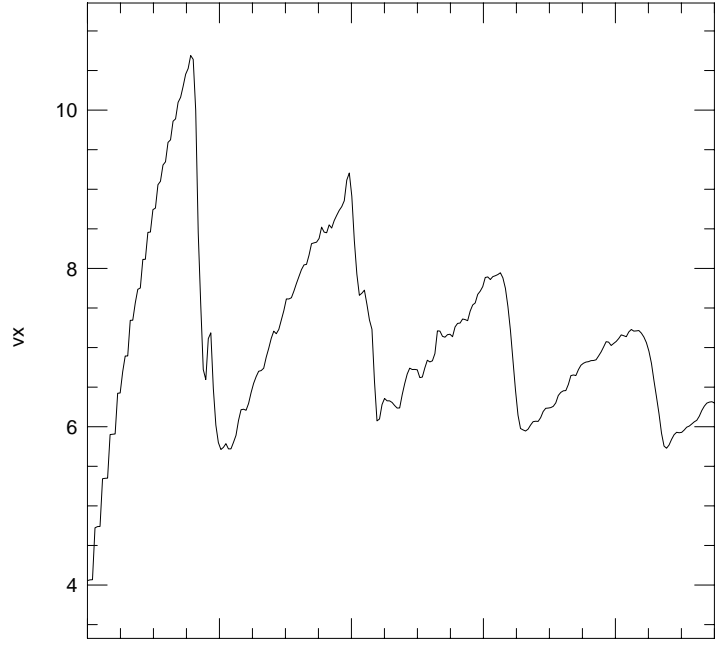
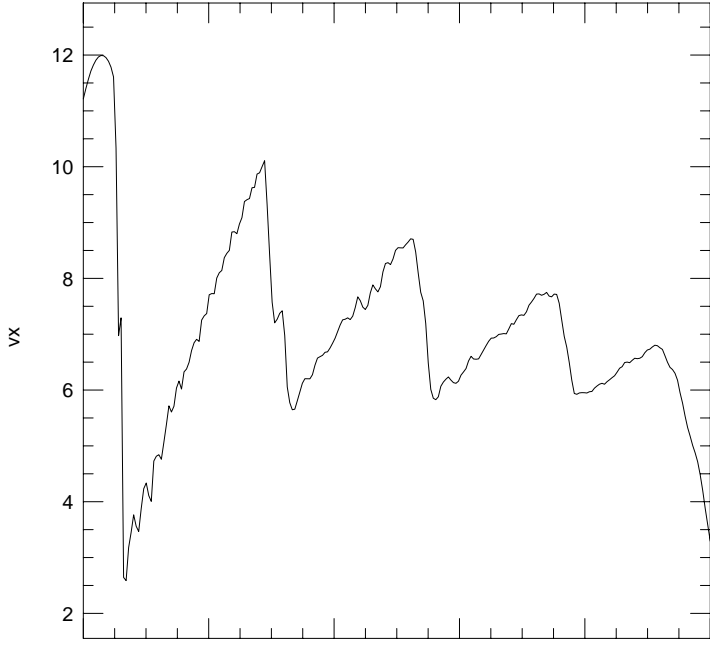
Figure 8: Longitudinal component of the momentum flux density (dashed lines) and the integrated momentum rate distribution (solid lines) for the jet of Figs. 5 to 7, at $t/t_d \simeq 9$, in different positions along the flow. At the positions: $x/R_j = -25, 2.5$, and 35, the lines trace the distributions profiles immediately behind the pulses; at the other positions, they trace the distributions at regions between the pulses. The momentum flux density, and the momentum rate scales can be calibrated using the markers in the top region of each plot - the marker for the momentum flux density corresponds to $\sim 1.7 \times 10^{-18}$ g cm $^{-3}$ (km s $^{-1}$) 2 , and the marker for the momentum rate corresponds to $\sim 1.2 \times 10^{-9} M_\odot$ yr $^{-1}$ km s $^{-1}$.

Figure 9: Mid-plane density contour (top) and velocity field distribution (bottom) for a pressure-confined radiatively cooling, steady-state jet propagating into an ambient medium with $T_a \sim 10^4$ K with constant velocity at injection $v_j \simeq 200$ km s $^{-1}$, and $M_a = 12$. The time depicted is $t/t_d \simeq 11 \simeq 2101$ yr, (where $t_d = R_j/c_a \approx 190$ yr, and $R_j = 10^{16}$ cm), and the jet has propagated for $\sim 100R_j \sim 0.3$ pc. The initial conditions for the jet are: $\eta = n_j/n_a = 3$, $n_a = 200$ cm $^{-3}$, and pressure equilibrium in the jet at the inlet, $\kappa = p_j/p_a = 1$. The distances are in units of $R_j = 10^{16}$ cm. The density lines are separated by a factor of 1.3 and the density scale covers the range $\sim (1.2 \times 10^{-1} - 0.4 \times 10^2) n_a$.

Figure 10: Propagation velocity of the leading working surface $v_{WS,o}$ (in units of $c_a = 16.6$ km s $^{-1}$), for the jet of Fig. 9. The distance is in units of $R_j = 10^{16}$ cm.

This figure "f1.gif" is available in "gif" format from:

<http://arxiv.org/ps/astro-ph/0012368v1>



This figure "f3.gif" is available in "gif" format from:

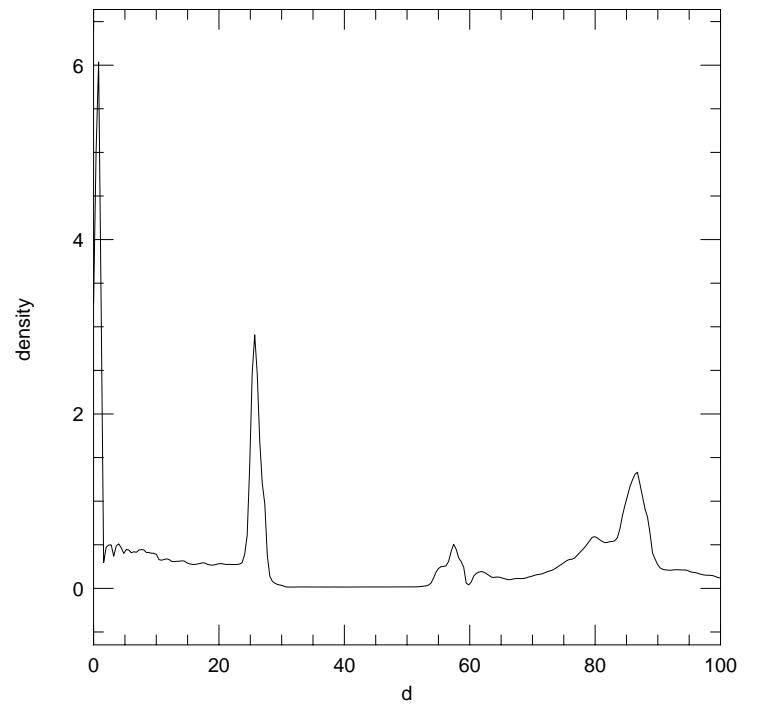
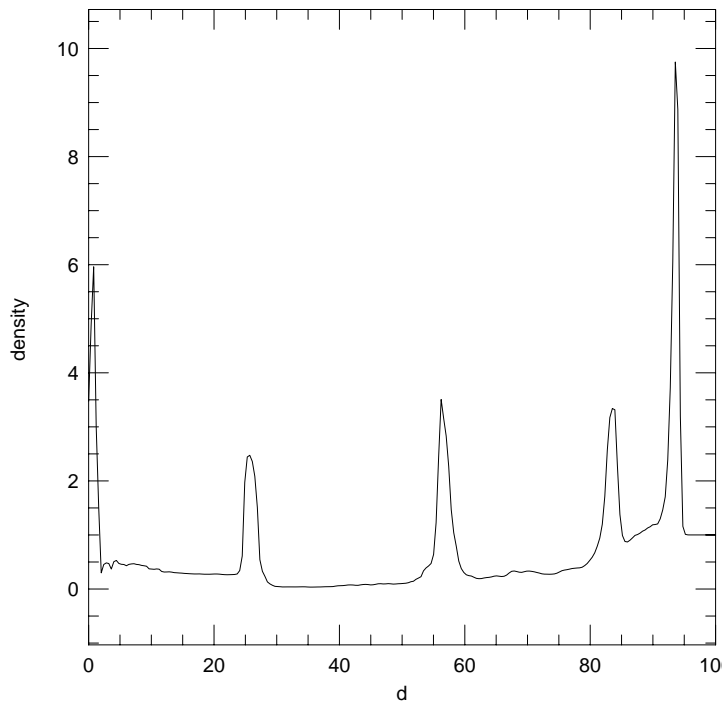
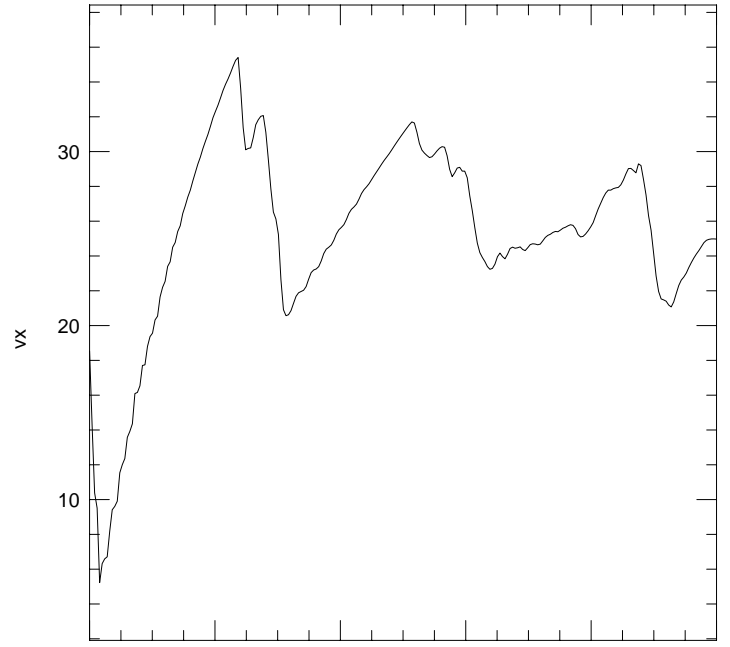
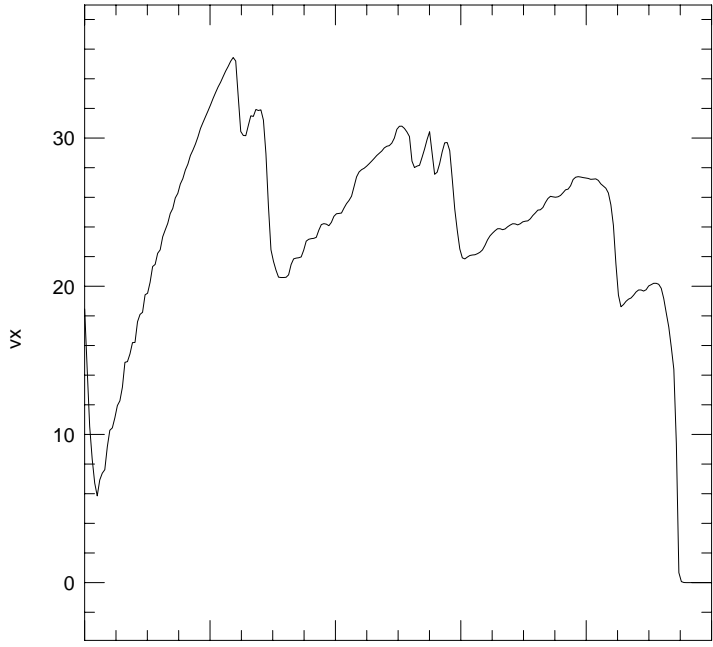
<http://arxiv.org/ps/astro-ph/0012368v1>

This figure "f4.gif" is available in "gif" format from:

<http://arxiv.org/ps/astro-ph/0012368v1>

This figure "f5.gif" is available in "gif" format from:

<http://arxiv.org/ps/astro-ph/0012368v1>



This figure "f7.gif" is available in "gif" format from:

<http://arxiv.org/ps/astro-ph/0012368v1>

This figure "f8.gif" is available in "gif" format from:

<http://arxiv.org/ps/astro-ph/0012368v1>

This figure "f9.gif" is available in "gif" format from:

<http://arxiv.org/ps/astro-ph/0012368v1>

This figure "f10.gif" is available in "gif" format from:

<http://arxiv.org/ps/astro-ph/0012368v1>